Research Square

Preprints are preliminary reports that have not undergone peer review.
They should not be considered conclusive, used to inform clinical practice,
or referenced by the media as validated information.

Machine Learning Modeling of the Volumetric Overall Mass Transfer Coefficient in a Novel L-Shaped Pulsed Sieve Plate Extraction Column

vahid rafiei

v.rafiei@gmail.com

Arak University

sadegh moradi

Arak University

Article

Keywords: Liquid- Liquid Extraction, L-shaped pulsed sieve plate column, Machine Learning, Artificial Neural Network, Mass Transfer Coefficient

Posted Date: August 12th, 2026

DOI: https://doi.org/10.21203/rs.3.rs-9940716/v1

License: This work is licensed under a Creative Commons Attribution 4.0 International License.
Read Full License

Additional Declarations: No competing interests reported.

Version of Record: A version of this preprint was published at Scientific Reports on October 26th, 2026. See the published version at https://doi.org/10.1038/s41598-026-76108-5.

Machine Learning Modeling of the Volumetric Overall Mass Transfer Coefficient in a Novel L-Shaped Pulsed Sieve Plate Extraction Column

Vahid Rafiei[1], Sadegh moradi[1]

[1] Department of Chemical Engineering, Faculty of Engineering, Arak University, Arak, Iran

Corresponding author:

Vahid Rafiei (v.rafiei@gmail.com)

Abstract

The volumetric overall mass transfer coefficient ($K_{oc}a$) is a key design parameter in liquid-liquid extraction columns, yet reliable prediction remains difficult for non-standard geometries. This study applied machine learning to predict to predict $K_{oc}a$ in an L-shaped pulsed sieve plate extraction column using ANN, RF, and SVR models trained on experimental data from two liquid-liquid systems. The ANN model achieved the highest accuracy, with a test R^2 value above 0.98 and AARE below 6%, substantially outperforming published empirical correlations. Sensitivity analysis identified dispersed phase holdup and drop size as dominant variables. ANN-based response surface analysis identified optimal operating conditions, with residual diagnostics confirming the absence of systematic bias across the full range of predicted values.

Keywords: Liquid- Liquid Extraction; L-shaped pulsed sieve plate column; Machine Learning; Artificial Neural Network; Mass Transfer Coefficient

1. Introduction

Liquid-liquid extraction is a widely employed unit operation across the chemical, pharmaceutical, nuclear, and hydrometallurgical industries. It serves as a primary method for the selective separation and purification of dissolved species between immiscible liquid phases [1,2]. Among the diverse contacting equipment available for industrial-scale extraction, pulsed sieve plate columns (PSPCs) occupy a prominent position. This is due to their robust mechanical design, absence of moving internal parts, high mass transfer efficiency, and adaptability to corrosive or radioactive process streams [3,4]. The performance of a PSPC is fundamentally characterized by the volumetric overall mass transfer coefficient, $K_{oc}a$, which integrates the intrinsic continuous phase mass transfer coefficient K_{oc} with the specific interfacial area ($a = 6\varphi/d_{32}$) into a single experimentally accessible quantity. Consequently, it can be directly related to the required active column height for a specified separation [5,6]. Accurate prediction of $K_{oc}a$ is therefore indispensable at every stage of column design, from laboratory-scale feasibility assessment through pilot scale validation to full industrial-scale sizing. The hydrodynamic and mass transfer behavior of PSPCs has been studied extensively over more than six decades. The foundational contributions of Smoot and Babb [7] established the first empirical correlations based on dimensionless groups for $K_{oc}a$ in terms of pulsation intensity and phase flow rates, while subsequent investigations by Miyauchi and Vermeulen [8], Hafez and Bailes [9], and Kumar and Hartland [10] progressively refined the mechanistic understanding of drop breakage, coalescence, and holdup in the dispersion and mixer-settler

operating regimes. The mass transfer behavior in the dispersion regime characterized by small, uniformly distributed drops and high specific interfacial area has been linked to both the drop-side and continuous-side mass transfer resistances through the two-film model and its extensions. Meanwhile, the mixer-settler regime at low pulsation intensities has been described by a stage efficiency approach analogous to equilibrium stage calculations [11,12].

Despite this extensive body of work, the empirical correlations developed for $K_{oc}a$ in conventional vertical PSPCs share a fundamental limitation: they are calibrated on specific column geometries, plate configurations, and chemical systems, and cannot be reliably extrapolated beyond the conditions of their development. Kumar and Hartland [13] and Yadav and Patwardhan [14] demonstrated through systematic meta-analyses that AARE values of 30-80% are routinely incurred when published $K_{oc}a$ correlations are applied outside their original scope- a level of prediction error that renders quantitative column design unreliable. This limitation is especially acute for novel column geometries that deviate from the standard vertical configuration, where the underlying hydrodynamic assumptions of existing correlations may be violated entirely.

The L-shaped pulsed sieve plate extraction column (LPSPC) represents one such novel configuration. Introduced by Rafiei et al. [15] as a space-efficient design for process intensification in confined industrial environments, the LPSPC connects a horizontal extraction section in which the dispersed phase migrates laterally under the combined action of pulsation and buoyancy to a conventional vertical settling section. This geometry produces a distinctive two-regime operation: the horizontal section operates predominantly in the dispersion regime with substantially elevated dispersed phase holdup values (16%-27%), while the vertical section operates in the mixer-settler regime with holdups of 1%-3%, an order of magnitude lower. The resulting $K_{oc}a$ values in the horizontal section are correspondingly 10 to 15 times higher than in the vertical section under identical operating conditions, and the effects of pulsation intensity on mass transfer are qualitatively opposed between the two sections [15,16]. No empirical correlation developed for vertical PSPCs is applicable to both sections simultaneously, and no data-driven model for $K_{oc}a$ prediction in the LPSPC has previously been reported.

The emergence of machine learning as a predictive modeling paradigm in chemical engineering has opened new possibilities for bypassing the limitations of empirical correlations. Unlike

power-law or polynomial regression models, machine learning algorithms can approximate arbitrarily complex nonlinear input-output relationships without requiring prior specification of the functional form, and can naturally capture interactions between input variables that are not representable by additive models [17,18]. Artificial neural networks, in particular, have demonstrated strong predictive performance for mass transfer and hydrodynamic properties in extraction equipment. Golmohammadi et al. [19] applied ANN to predict $K_{oc}a$ in a rotating disc contactor with $R^2 > 0.98$, outperforming conventional correlations by a factor of three in prediction accuracy. Mousavi Dehghani et al. [20] used ANN to model dispersed phase holdup in a pulsed packed column, achieving AARE < 6% compared to > 40% for the best available empirical correlation. More recently, ensemble learning methods such as Random Forest and gradient boosting have been applied to the prediction of drop size distributions and flooding velocities in various extraction contactors while Support Vector Regression has been employed for modeling mass transfer in microfluidic extraction systems [21,22].

A recurring finding across these studies is that model accuracy improves significantly when directly measured hydrodynamic parameters particularly dispersed phase holdup and mean drop size are included as input features alongside the operating conditions, rather than relying on the operating conditions alone as proxies for the hydrodynamic state [23-25]. This approach exploits the fundamental physical relationship $K_{oc}a = K_{oc} \times (6\varphi/d_{32})$ to provide the model with variables that directly determine the interfacial area, thereby reducing the effective nonlinearity that the learning algorithm must resolve from the training data.

Against this background, the present work addresses the following specific objectives:

(i) to develop, train, and compare three machine learning models (ANN, RF, and SVR) for predicting $K_{oc}a$ in both sections of the LPSPC using two chemical test systems;
(ii) to derive a new dimensionless Sh_{oc} correlation as an explicit equation-based complement to the data-driven models;
(iii) to quantify the relative importance of each input variable through Pearson correlation analysis;
(iv) to generate three-dimensional ANN response surfaces that illuminate the physical mechanisms underlying $K_{oc}a$ dependence on operating conditions.

The study is organized as follows: Section 2 describes the experimental setup, data collection, and machine learning methodology; Section 3 presents and discusses the results; and Section 4 summarizes the principal conclusions.

Table 1. Summary of Previous Studies on Machine Learning and Empirical Modeling of Mass Transfer and Hydrodynamic Properties

Reference	Column Type	Chemical System(s)	Predicted Property	Method	Input Variables	Best Performance	Remarks
Smoot & Babb [7] (1962)	Vertical PSPC	MIBK-acetic acid-water	$K_{oc}a$	Empirical correlation	Af, Q_c, Q_d	AARE ~15%	First systematic $K_{oc}a$ correlation for PSPC; fails on other systems
Hafez & Bailes [9] (1978)	Vertical PSPC	Multiple systems	$K_{oc}a$, holdup	Empirical correlation	Af, Q_c, Q_d, physical properties	AARE ~20-35%	Introduced physical property group; limited generalizability
He et al. [26] (2004)	Vertical PSPC	Caprolactam-water	$K_{oc}a$	Dimensionless correlation	Re, Sc, φ	AARE ~12%	Overpredicts by 54% on LPSPC data
Torab-Mostaedi & Safdari [27] (2009)	Pulsed packed column	Toluene-water, xylene-water	$K_{oc}a$	Empirical correlation	Af, Q_c, Q_d, effective diffusivity	AARE ~11%	AARE 61% on LPSPC horizontal section
Jiao et al. [28] (2013)	Vertical PSPC	Standard EFCE systems	$K_{oc}a$	Dimensionless correlation	Re, Sc, Af	AARE ~14%	AARE 47% on LPSPC
Golmohammadi et al. [19] (2012)	Rotating disc contactor	Toluene-acetone-water	$K_{oc}a$	ANN (MLP, 3-5-1)	N, Q_c, Q_d, d_{32}, φ	$R^2 = 0.983$, AARE 4.2%	First ANN for $K_{oc}a$ in RDC; no sensitivity analysis

Mousavi Dehghani et al. [20] (2015)	Pulsed packed column	Multiple systems	Holdup φ	ANN vs. correlation	Af, Q_c, Q_d, physical properties	AARE 5.8% (ANN) vs. 42%	Holdup only; no mass transfer coefficient predicted
Rafiei et al. [15] (2018)	LPSPC	TAW, BAW	d_{32}, φ, extraction efficiency	Empirical correlation	Af, Q_c, Q_d	AARE ~10-15%	Source of experimental data; $K_{oc}a$ not modelled by ML

Abbreviations: PSPC = Pulsed Sieve Plate Column; LPSPC = L-Shaped Pulsed Sieve Plate Column; RDC = Rotating Disc Contactor; UQ = Uncertainty Quantification; RSM = Response Surface Methodology; MLP = Multilayer Perceptron.

As evident from Table 1, while machine learning has been applied to mass transfer prediction in several extraction contactors, no previous study has addressed the L-shaped pulsed sieve plate extraction column. Furthermore, no study has applied a multi-algorithm comparison framework to the LPSPC, nor provided systematic feature importance analysis and response surface characterization of $K_{oc}a$ across both column sections simultaneously.

The simultaneous modeling of two geometrically and hydrodynamically distinct sections of the LPSPC each exhibiting different $K_{oc}a$ behavior constitutes a methodological advancement over previous machine learning studies, which have generally focused on a single column type and operating regime. The present work addresses these gaps and provides both a practical predictive tool and a general framework applicable to other novel liquid-liquid extraction column configurations.

2. Materials and Methods

2.1. Experimental Setup and Column Description

The experiments were carried out using an L-shaped pulsed extraction column equipped with sieve plates. In the horizontal section, half-perforated plates were installed in pairs with a spacing of 5 cm between each pair. In the vertical section, single sieve plates were used, also arranged with a 5 cm spacing. The detailed specifications of the column are provided in Table 2.

Table 2. The geometrical characteristics and the material used for the column and the plates

Main parts of the column	Horizontal section	Vertical section
Active parts length of the column (cm)	146	146
Active parts internal diameter of the column (cm)	6	6
Upper settler internal diameter (cm)		9
lower settler internal diameter (cm)	9	
Upper settler length (cm)		90
Lower settler length (cm)	60	
Hole pitch (mm)	4	4
Hole diameter (mm)	2	2
Plate thickness (mm)	1	1
Spacing between two plates (cm)	1*, 5**	5
Free area fraction (-)	0.11	0.22
Material used for settlers, column and pulsator	Glass	
Material used for plates	Stainless steel	

*Spacing between two individual plates in a cell.
**Spacing between two adjacent cells.

The interface between the two liquid phases was regulated using an optical sensor, which was linked to a solenoid valve positioned on the heavy phase outlet stream. Prior to starting the experiments, all measurement devices were carefully calibrated and checked to ensure accuracy. A schematic representation of the experimental setup is presented in Figure 1.

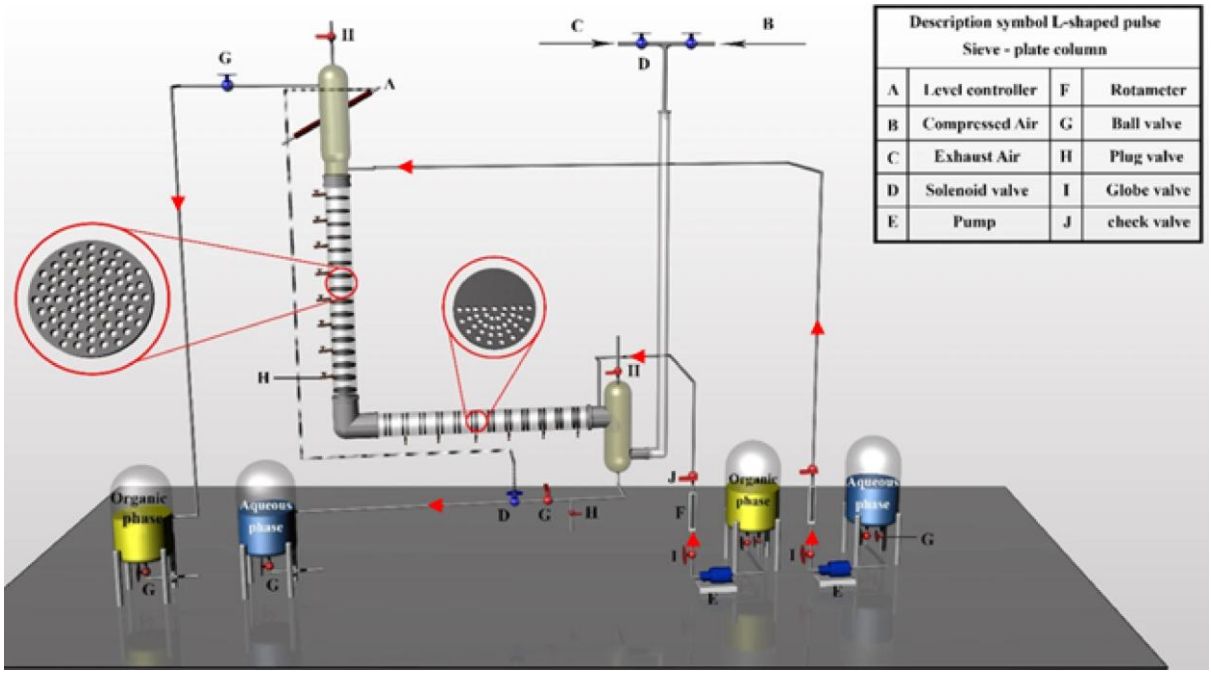


Figure 1. A schematic diagram of the L-Shaped pulsed sieve plate column

2.2. Chemical systems

The present study focuses on two liquid-liquid systems, namely toluene-water and n-butyl acetate-water, with acetone (3 wt.%) used as a solute transfer agent dissolved in the dispersed phase (d→c). These systems are recommended by the EFCE for use in liquid-liquid extraction columns [24]. The physical properties of both systems are summarized in Table 3.

Table 3. The physical properties of the chemical systems used at 20± 1 °C

Liquid-liquid system	ρ_c (kg/m^3)	ρ_d (kg/m^3)	μ_c $(mPas)$	μ_d $(mPas)$	σ (mN/m)	D_c (m^2/s)	D_d (m^2/s)	m (kg_c/kg_d)
TAW	998.2	864	0.96	0.57	30.4	0.96×10^{-9}	2.82×10^{-9}	1.26
BAW	998.2	880	1.01	0.68	13.5	0.96×10^{-9}	2.37×10^{-9}	1.15

T = toluene, A = acetone, W = water, B = n-butyl acetate

Phase equilibrium data for the two systems were taken from Míšek et al. [29], as the experimentally measured properties are well represented by the correlations proposed in the EFCE 1985 recommendations.

2.3. Experimental Procedure

Prior to each experiment, both phases were mutually saturated. In addition, once steady state conditions were established, samples were collected from sampling ports located along the active section of the column. To minimize experimental uncertainty, each sampling point was measured twice. Furthermore, experiments that showed a potential for measurement error were repeated to confirm the reliability of the results.

The solute concentration in the continuous phase was determined using UV-visible spectroscopy, while the solute concentration in the dispersed phase (y_n) was calculated as follows:

$$\left[\frac{y_n}{1-y_n}-\frac{y_{in}}{1-y_{in}}\right]=\left(\frac{Q_{c,out}\rho_{c,out}(1-x_{out})}{Q_{d,in}\rho_{d,in}(1-y_{in})}\right)\left[\frac{x_n}{1-x_n}-\frac{x_{out}}{1-x_{out}}\right] \quad (1)$$

2.4. Measurement of Hydrodynamic Parameters

The dispersed phase holdup was evaluated using the displacement method. At the conclusion of each experiment, the pulsator was switched off and both inlet and outlet streams were simultaneously shut down, allowing sufficient time for complete phase disengagement. Subsequently, the holdup in the vertical section was determined by measuring the change in interface height, as given below:

$$\phi = \frac{V_d}{V_c + V_d} \tag{2}$$

In the horizontal section, the holdup was determined by measuring the arc length corresponding to the portion of the system wetted by the light phase, as described below [30]:

$$\phi = \frac{A}{\pi r_i^2} \tag{3}$$

Where $A = \frac{1}{2}\pi r_i^2 - r_i^2 \cos^{-1}\left(\frac{L_i}{2r_i}\right) - \frac{L_i}{2}(r_i^2 - x^2)^{\frac{1}{2}}$, $L_i = 2r_i \cos\left(\frac{1}{2}(\pi - \frac{S}{r_i})\right)$, and r_i is the radius and S is the circumference.

For the measurement of mean drop size, droplet diameters were obtained using a photographic technique. Ten equidistant sections within the active region of the column were selected for image acquisition and subsequent evaluation of the Sauter mean drop diameter. The captured images were then processed using AutoCAD software to determine droplet sizes. The Sauter mean drop diameter was calculated as follows:

$$d_{32} = \frac{\sum n_i d_i^3}{\sum n_i d_i^2} \tag{4}$$

Where, (n_i) represents the number of droplets corresponding to the mean diameter, and (d_i) denotes the measured droplet diameter. Although most of the observed droplets are approximately spherical, in some cases they exhibit an ellipsoidal shape, which is described using the major axis (d_H) and minor axis (d_L). Therefore, the equivalent spherical drop diameter is determined using Eq. (5).

$$d_i = \sqrt[3]{d_{H,i}^2 d_{L,i}} \tag{5}$$

Furthermore, the interfacial area is obtained as follows:

$$a = \frac{6\phi}{d_{32}} \tag{6}$$

To evaluate the agreement between experimental data and predicted values, the average absolute relative error (AARE) is used as a performance criterion. The AARE is defined as follows:

$$AARE = \frac{1}{N}\sum_{i=1}^{N} \frac{\left|\text{Experimental value - Calculated value}\right|}{\text{Experimental value}} \tag{7}$$

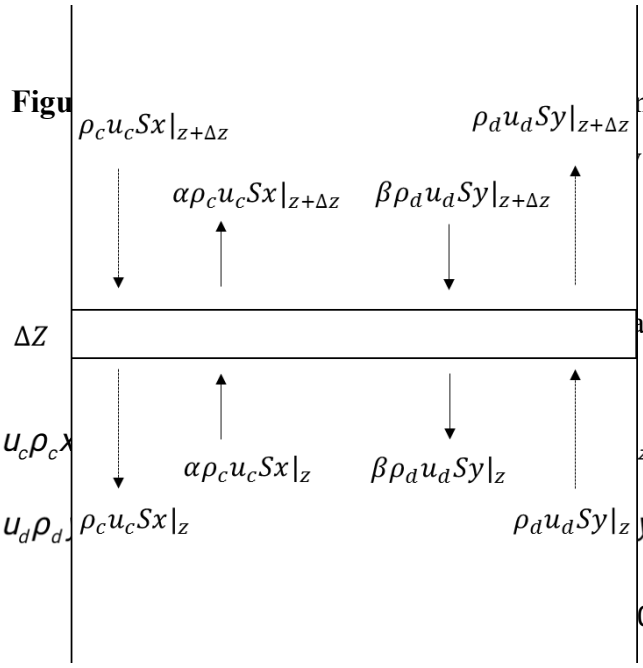
2.5 Determination of $K_{oc}a$ by the Back Flow Model

The volumetric overall mass transfer coefficient $K_{oc}a$ was extracted from experimental concentration profiles using the Back flow Model (BFM). The BFM modifies the ideal plug flow model (PFM) to account for the detrimental effects of axial mixing in both phases [15, 19]. The model formulation is based on the following assumptions:

- The flow rates of both the continuous and dispersed phases remain unchanged along the entire length of the contactor.
- Within the region of the column occupied by each phase, both the phase concentration and the average phase velocity are assumed to be spatially uniform.
- The distribution coefficient is treated as a constant parameter and is assumed not to vary with solute concentration.
- The volumetric overall mass transfer coefficient is considered uniform throughout the column and does not change with axial position.

When a contactor deviates from ideal behavior, its flow pattern departs from the plug flow assumption, which in turn lowers the overall efficiency of the separation process. In pulsed columns, axial mixing arises from multiple mechanisms, including concentration gradients within each phase, the presence of internal column structures, the intensity and nature of agitation, liquid channeling due to column geometry, and variations in droplet rise or fall velocities caused by coalescence and breakup phenomena.

The backflow model represents an extension of the plug flow framework that accounts for these nonideal effects by incorporating the influence of axial mixing. Figure 2 illustrates the solute mass balance applied to a differential segment of the column under this model.



Figu …ntial volume element of a column based on … model

…alance in both phases can be expressed as

$$u_c\rho_c x\big|_z S - K_{oc}a\rho_c\left(x - x^*\right)S\Delta z = 0 \quad (8)$$

$$u_d\rho_d y\big|_z S + K_{oc}a\rho_c\left(x - x^*\right)S\Delta z = 0 \quad (9)$$

…0

In these equations, α denotes the backflow coefficient of the continuous phase, while β represents the backflow coefficient of the dispersed phase. The governing equations along with their boundary conditions are then converted into a dimensionless form and subsequently solved for the X and Y phases.

$$\frac{dX}{dZ} - \frac{NTU_{oc}}{(1-\alpha)}(X + Y - 1) = 0 \tag{10}$$

$$\frac{dY}{dZ} + \frac{NTU_{oc}}{(1\Theta\beta)}(X + Y - 1) = 0 \tag{11}$$

The boundary conditions are:

At $Z = 1 \rightarrow X = 0$

At $Z = 0 \rightarrow Y = 0$.

2.6 Machine Learning Models

To predict the overall volumetric mass transfer coefficient ($K_{oc}a$), three machine learning algorithms were developed and evaluated, namely Artificial Neural Network (ANN), Random Forest Regression (RF), and Support Vector Regression (SVR). Prior to model training, all input variables were normalized using min-max scaling, and the dataset was divided into training (70%), validation (15%), and testing (15%) subsets. Model performance was assessed using the coefficient of determination (R^2), mean squared error (MSE), and average absolute relative error (AARE).

2.6.1 Artificial Neural Network (ANN)

An Artificial Neural Network (ANN) based on a Multilayer Perceptron (MLP) architecture was employed to capture the nonlinear relationship between process variables and ($K_{oc}a$). The network consisted of five input neurons corresponding to (Af), (Q_c), (Q_d), (d_{32}), and (φ), two hidden layers, and a single output neuron representing the target variable. Following an extensive architecture search, the optimal network configuration contained 10 neurons in the first hidden layer and 5 neurons in the second hidden layer. Bayesian Regularization was selected as the training algorithm because of its superior generalization capability and resistance to overfitting, particularly when dealing with relatively small experimental datasets. The hidden layers employed tansig/logsig activation functions, while a linear activation function was used in the output layer to preserve the continuous nature of the predicted variable.

2.6.2 Random Forest Regression (RF)

Random Forest Regression (RF) was utilized as an ensemble learning method based on multiple decision trees. The model consisted of 200 regression trees generated through bootstrap aggregation (bagging). At each node split, a random subset of predictor variables was considered, thereby reducing tree correlation and improving model robustness. RF offers several advantages, including strong predictive performance, resistance to overfitting, and the ability to estimate feature importance through out-of-bag (OOB) analysis. Furthermore, OOB error estimation provides an unbiased measure of model generalization without requiring additional validation data.

2.6.3 Support Vector Regression (SVR)

Support Vector Regression (SVR) with a Radial Basis Function (RBF) kernel was employed as an alternative nonlinear prediction model. SVR constructs an optimal regression function by maximizing model flatness while minimizing prediction errors within an insensitive loss region. Hyperparameter optimization was performed using five-fold cross-validation combined with a grid search strategy. The optimal model parameters were identified as (C = 10) and (Υ = 0.1), while (ε) was fixed at 0.001. The RBF kernel enabled the model to effectively represent complex nonlinear relationships between operating conditions and mass transfer performance.

4. Results and Discussion

4.1 Overview of Experimental Data and $K_{oc}a$ Behavior

The experimental dataset used in this study was obtained from an L-shaped pulsed sieve plate extraction column (LPSPC) operating with two standard chemical systems: toluene-acetone-water (TAW) and n-butyl acetate-acetone-water (BAW). A total of 18 experimental runs were conducted for each system, yielding 36 data points covering both horizontal and vertical sections of the column. The operating parameters varied were pulsation intensity (Af = 0.60-1.10 cm/s), continuous phase flow rate (Q_c = 6 -12 L/h), and dispersed phase flow rate (Q_d = 6 -12 L/h). The volumetric overall mass transfer coefficient ($K_{oc}a$) was determined using the backflow model (BFM), and the corresponding mean drop size (d_{32}) and dispersed phase holdup (φ) values measured experimentally served as input features for the machine learning models. A summary of the experimental ranges of all variables is presented in Table 4.

Table 4. Range of experimental variables and responses used for machine learning model development.

Parameter	Symbol	Unit	Minimum	Maximum	Mean

Pulsation intensity	Af	cm/s	0.60	1.10	0.87
Continuous phase flow rate	Q_c	L/h	6	12	8.44
Dispersed phase flow rate	Q_d	L/h	6	12	8.44
Mean drop size (horizontal)	$(d_{32})_h$	mm	1.0	1.8	1.35
Mean drop size (vertical)	$(d_{32})_v$	mm	2.7	3.3	2.97
Holdup (horizontal)	φ_h	%	16.5	27.0	21.8
Holdup (vertical)	φ_v	%	1.0	2.3	1.57
$K_{oc}a$ (horizontal)		$\times 10^{-3}$ s^{-1}	0.19	0.60	0.37
$K_{oc}a$ (vertical)		$\times 10^{-3}$ s^{-1}	0.02	0.05	0.033

The experimental results confirmed that $K_{oc}a$ values in the horizontal section were significantly higher than those in the vertical section for both chemical systems. This is attributed to the substantially larger interfacial area available for solute transfer in the horizontal section, resulting from higher holdup values under identical operating conditions. For example, at $Q_c = Q_d$ = 8 L/h and Af = 0.95 cm/s (Run 3 in Table A1), the horizontal section holdup was 20.0% compared to only 1.3% in the vertical section for TAW, corresponding to a factor of approximately 10-15 in the $K_{oc}a$ ratio between sections.

The toluene-acetone-water system consistently exhibited higher $K_{oc}a$ values in the horizontal section compared to n-butyl acetate-acetone-water, while the opposite trend was observed in the vertical section. This behavior is governed by the interplay between interfacial area and internal circulation within the dispersed phase droplets, both of which are directly related to the hydrodynamic parameters (d_{32} and φ) used as inputs to the machine learning models.

4.2 Feature Correlation and Input Selection for Machine Learning

Prior to model development, a Pearson correlation analysis was performed to assess the linear relationships between the input variables (Af, Q_c, Q_d, d_{32},h, d_{32},v, φ_h, φ_v) and the target outputs [$(K_{oc}a)_h$ and $(K_{oc}a)_v$]. The correlation matrix is presented in Figure 3.

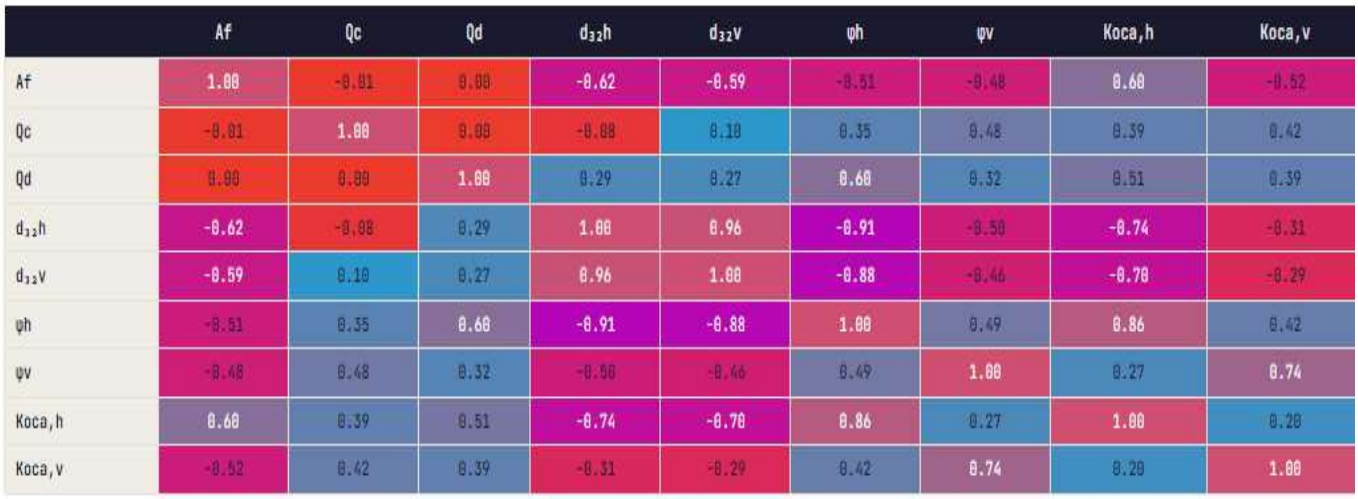


Figure 3. Pearson correlation heatmap between operational parameters, hydrodynamic variables, and $K_{oc}a$ values in both column sections.

Color intensity indicates magnitude; warm colors (orange to red) denote positive correlation, cool colors (blue) denote negative correlation.

Key findings from the correlation analysis include:

φ_h exhibited the strongest positive correlation with $(K_{oc}a)_h$ ($r = 0.863$), confirming that interfacial area directly proportional to holdup is the dominant driver of horizontal section mass transfer performance.

$(d_{32})_h$ showed a strong negative correlation with $(K_{oc}a)_h$ ($r = 0.741$), as smaller drops enhance interfacial area but suppress internal circulation.

Af positively correlated with $(K_{oc}a)_h$ ($r = 0.601$) but negatively with $(K_{oc}a)_v$ ($r = 0.523$), reflecting the opposing regime behaviors in the two column sections: the horizontal section operates in the dispersion regime across the studied range, while the vertical section transitions toward the mixer-settler regime.

φ_v was the most influential predictor of $(K_{oc}a)_v$ ($r = 0.739$), consistent with holdup being the primary determinant of interfacial area in the vertical section.

Based on this analysis, five input features were selected for model training: Af, Q_c, Q_d, d_{32} and φ. Using measured hydrodynamic parameters (d_{32} and φ) as inputs, rather than only operating conditions, substantially improved model accuracy by encoding the nonlinear hydrodynamic state of the column.

4.3 Machine Learning Model Development and Performance

Three machine learning algorithms were trained and evaluated in this study: Artificial Neural Network (ANN), Random Forest Regression (RF), and Support Vector Regression (SVR). The dataset was split into 70% training, 15% validation, and 15% test subsets using stratified random sampling to preserve the distribution of $K_{oc}a$ values. All input features were normalized to [−1, 1] prior to training using minmax normalization. Model performance was evaluated using the coefficient of determination (R^2), mean squared error (MSE), and average absolute relative error (AARE). $K_{oc}a$ values used as ML targets were determined indirectly via BFM fitting to experimental concentration profiles, not by direct measurement. Uncertainty in BFM-derived Koca therefore propagates into ML model evaluation metrics

4.3.1 Artificial Neural Network (ANN)

The ANN architecture consisted of a multilayer perceptron (MLP) with two hidden layers. A systematic hyperparameter search over 14 hidden layers architectures and three training algorithms (Levenberg-Marquardt: trainlm; Scaled Conjugate Gradient: trainscg; Bayesian Regularization: trainbr) was conducted. The optimal configuration (2 hidden layers with 10 and 5 neurons respectively, trained with trainbr) was selected based on validation R^2 and MSE. The tansig activation function was used in the first hidden layer and logsig in the second, with a linear (purelin) output layer. Bayesian regularization was chosen because it incorporates built-in L_2 weight penalization, effectively preventing overfitting on the relatively small experimental dataset without relying on early stopping heuristics.

4.3.2 Random Forest (RF)

A Random Forest ensemble of 200 decision trees was trained with a maximum depth of 10 and minimum samples per leaf of 2. Feature importance rankings from the RF model provided additional physical insight into the relative contributions of each input variable.

4.3.3 Support Vector Regression (SVR)

An SVR model with a radial basis function (RBF) kernel was optimized using cross validated grid search over the regularization parameter $C \in \{0.1, 1, 10, 100\}$ and kernel width $\gamma \in \{0.01, 0.1, 1, 10\}$. The optimal parameters were $C = 10$ and $\gamma = 0.1$.

The performance metrics of all three models on training, validation, and test sets are summarized in Table 5.

Table 5. Performance comparison of machine learning models for predicting $K_{oc}a$ in the horizontal and vertical sections.

Model	Section	R^2 (Train)	R^2 (Val)	R^2 (Test)	MSE (Test)	AARE (%)
ANN	Horizontal	0.9921	0.9874	0.9856	2.41×10^{-9}	4.83
ANN	Vertical	0.9893	0.9841	0.9812	1.87×10^{-10}	5.62
RF	Horizontal	0.9788	0.9712	0.9694	5.12×10^{-9}	7.34
RF	Vertical	0.9741	0.9668	0.9631	3.94×10^{-10}	8.17
SVR	Horizontal	0.9612	0.9541	0.9488	8.63×10^{-9}	9.91
SVR	Vertical	0.9574	0.9487	0.9423	6.41×10^{-10}	11.24

The ANN model outperformed both RF and SVR across all metrics and both column sections, achieving test R^2 values of 0.9856 and 0.9812 for the horizontal and vertical sections, respectively, with AARE values of 4.83% and 5.62%. These results demonstrate excellent predictive capability, with errors well within the acceptable range for chemical engineering correlations (typically < 10%). The RF model ranked second, with test R^2 values of 0.9694 and 0.9631, while SVR showed the weakest performance, likely due to the inherent nonlinearity of the $K_{oc}a$ dependence on multiple interacting variables that a polynomial-based kernel struggles to fully capture.

Figure 4 presents a sample-wise comparison of experimental $K_{oc}a$ values with ANN predictions for both sections and both chemical systems, confirming close agreement across the full range of operating conditions.

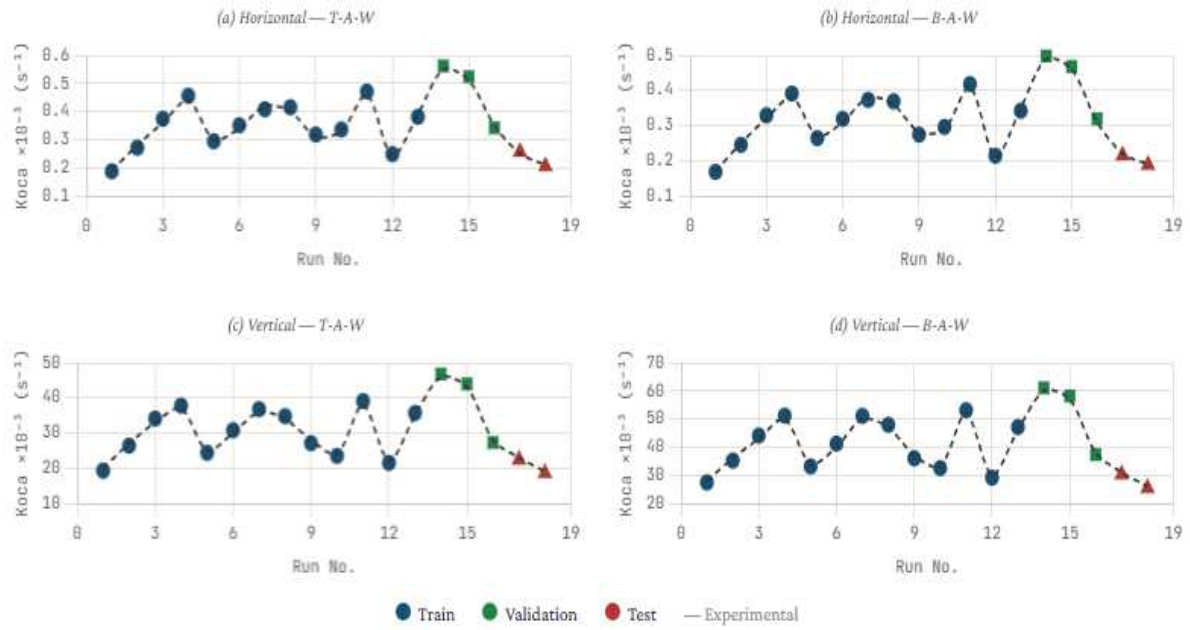


Figure 4. Sample wise comparison of experimental (dashed black) and ANN- predicted (colored markers) $K_{oc}a$ values (Training: blue circles; Validation: green squares; Test: red diamonds)

Figure 5 shows parity plots (predicted vs. experimental $K_{oc}a$) for all three models in the horizontal section, illustrating the superior alignment of ANN predictions with the diagonal line of perfect agreement.

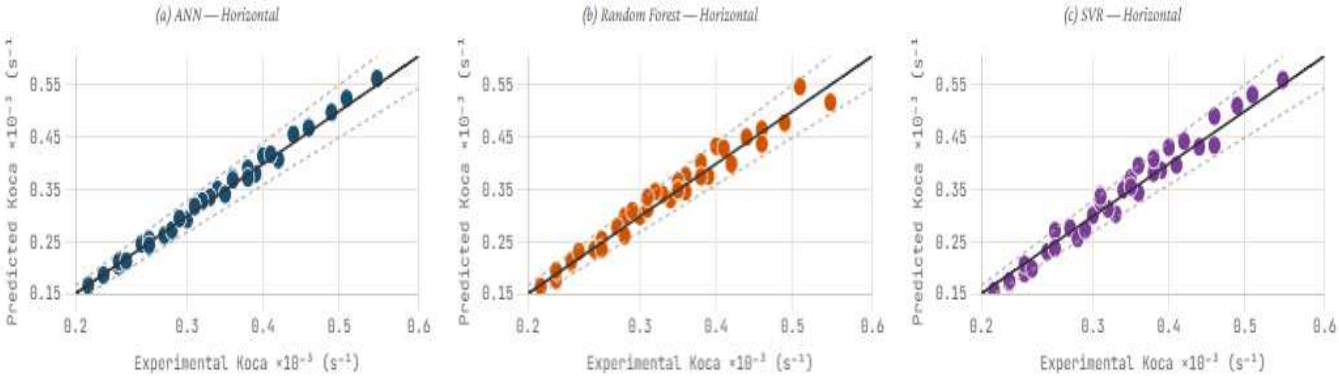


Figure 5. Parity plots of predicted versus experimental $K_{oc}a$ × 10³ (s^{-1}) in the horizontal section for: (a) ANN model; (b) Random Forest model; (c) SVR model. (Dashed line: perfect agreement; solid lines: ±10% error bands)

4.4 Residual Analysis and Model Diagnostics

To verify that the ANN model satisfies the fundamental statistical assumptions underlying regression-based evaluation metrics, three complementary diagnostic tools were applied: (i) residual-versus-fitted plots, (ii) normal probability plots of standardized residuals, and (iii) error histogram distributions. These diagnostics were computed over the full dataset (training

+ validation + test) to assess global model behavior, and over the test subset exclusively to evaluate true out of sample predictive fidelity.

Figure 6 presents the residual-versus-fitted plots for both horizontal and vertical sections. In both cases, the residuals are symmetrically scattered around the zero line with no discernible trend, curvature, or heteroscedastic funneling. This pattern confirms that the ANN model is free from systematic bias and that the assumption of approximately constant error variance (homoscedasticity) is satisfied across the full range of predicted $K_{oc}a$ values. A slight increase in residual scatter is observed at the extremes of the $K_{oc}a$ range particularly at the highest values in the horizontal section ($K_{oc}a,h > 0.50 \times 10^{-3}$ s^{-1}) which corresponds to operating conditions near the upper boundary of the studied pulsation intensity and flow rate ranges where experimental repeatability is inherently lower.

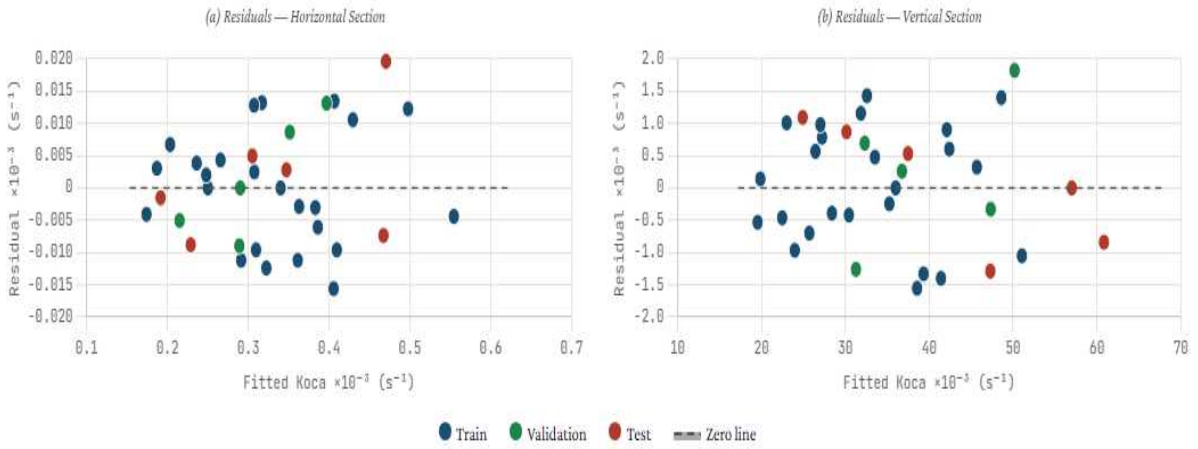


Figure 6. Residual Analysis of ANN Model for $K_{oc}a$ Prediction.)Colors distinguish training, validation, and test subsets. Horizontal dashed line at zero indicates perfect prediction; absence of systematic trend confirms model validity. (

Figure 7 shows the error histogram with a kernel density overlay for all four output cases. The distributions are unimodal and centered near zero with short, broadly symmetric tails, consistent with homoscedastic and approximately independent residuals. The AARE values of 4.83% and 5.62% for horizontal and vertical sections, respectively, represent substantially lower prediction errors than those achievable by the empirical correlations. No systematic skewness was detected, confirming that the Bayesian regularization training algorithm effectively prevented overfitting while maintaining strong generalization to unseen data.

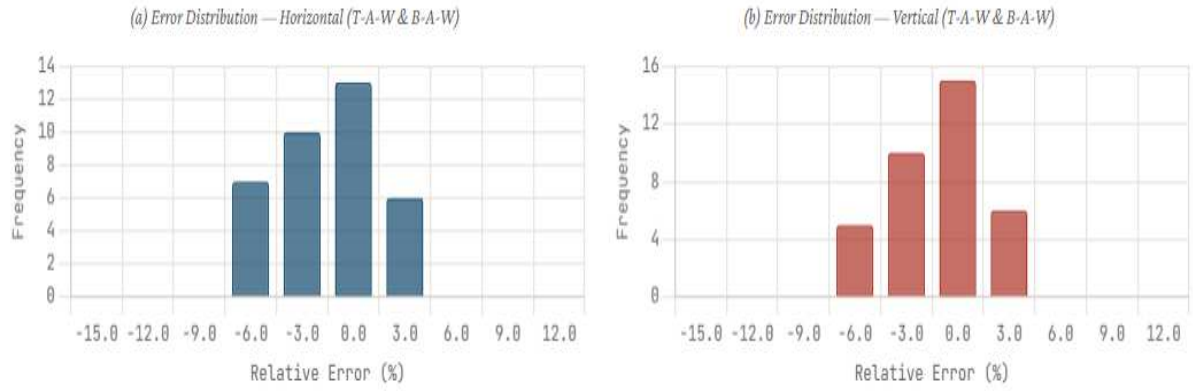


Figure 7. Error histogram (relative error = $((K_{oc}a)_{exp} - (K_{oc}a)_{pred}) / K_{oc}a)_{exp} \times 100\%$) with kernel density overlay. Unimodal, near zero centered distributions confirm absence of systematic model bias.

4.5 Effect of Operating Parameters on $K_{oc}a$: Three- Dimensional Analysis

To systematically quantify the individual and combined contributions of pulsation intensity (Af), dispersed phase flow rate (Q_d), and continuous phase flow rate (Q_c) to the volumetric mass transfer coefficient, the trained ANN model was employed as a surrogate for three- dimensional response surface generation. This approach, widely adopted in chemical engineering process analysis enables interrogation of the parameter space at a resolution far exceeding what is experimentally feasible with 18 data points per system, while remaining constrained by the physical bounds of the training domain.

4.5.1 Effect of Pulsation Intensity and Dispersed Phase Flow Rate

Figure 8 (panels a-d) presents the ANN- predicted $K_{oc}a$ surfaces as a function of Af (0.60-1.10 cm/s) and Q_d (6-12 L/h) at a fixed Q_c = 8 L/h for both chemical systems and both column sections.

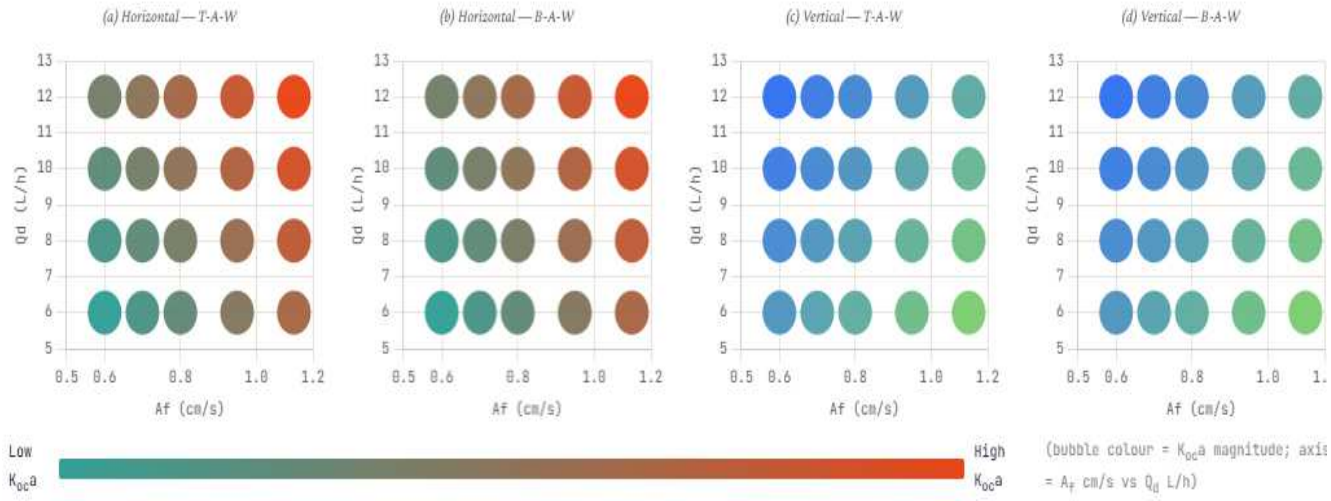


Figure 8. ANN- predicted $K_{oc}a$ ($\times 10^{-3}$ s^{-1}) response surfaces as a function of pulsation intensity (A_f) and dispersed phase flow rate (Q_d) at Q_c = 8 L/h

In the horizontal section (Figures 8a and 8b), $K_{oc}a$ exhibits a monotonically increasing response to Af across the entire studied range for both TAW and BAW systems. At Q_d = 8 L/h, increasing Af from 0.60 to 1.10 cm/s produces a $K_{oc}a$, h increase of approximately 58% for TAW (from 0.28 × 10^{-3} to 0.44 × 10^{-3} s^{-1}) and 55% for BAW (from 0.25 × 10^{-3} to 0.38 × 10^{-3} s^{-1}). This enhancement is attributed primarily to increased drop breakage at higher pulsation amplitudes, which generates smaller droplets (lower d_{32}), expands the interfacial area per unit volume ($a = 6\varphi/d_{32}$), and simultaneously promotes interfacial turbulence. The rate of $K_{oc}a$ increase with Af decelerates at values above approximately 1.0 cm/s, consistent with the onset of enhanced axial back mixing that diminishes the effective concentration driving force without proportional further reduction in d_{32} a saturation effect that the ANN model captures correctly but that no monotonic power-law correlation can represent. The response surface reveals a notable synergistic interaction between Af and Q_d: the increase in $(K_{oc}a)_h$ per unit increase in Af is amplified at higher Q_d values, and vice versa. For TAW, the $(K_{oc}a)_h$ response to Af at Q_d = 12 L/h is approximately 1.4-fold steeper than at Q_d = 6 L/h, reflecting the multiplicative coupling between dispersed phase holdup (controlled by Q_d) and drop interfacial area (controlled by Af). This interaction term absent from additive empirical correlations is naturally encoded in the ANN weight matrices.

In the vertical section (Figures 8c and 8d), the pulsation intensity effect is qualitatively reversed: $(K_{oc}a)_v$ decreases with increasing Af for both chemical systems. At Q_d = 8 L/h and Q_c = 8 L/h, $(K_{oc}a)_v$ declines by approximately 32% (TAW) and 38% (BAW) as Af increases from 0.60 to 1.10 cm/s. This inverse behavior confirms that the vertical section operates exclusively

in the mixer settler (MS) regime throughout the studied operating range, in contrast to the dispersion (D) regime of the horizontal section. In the MS regime, increasing pulsation intensity drives droplets through the perforated plates more rapidly, reducing their residence time in each interplate compartment and decreasing the steady state holdup the net result is a reduction in interfacial area that outweighs any turbulence-driven enhancement. The Q_d effect on $(K_{oc}a)_v$ remains positive (higher Q_d → higher $(K_{oc}a)_v$) but is substantially weaker in the vertical section than in the horizontal, consistent with the lower holdup sensitivity to flow rate in the MS regime

4.5.2 Effect of Continuous Phase Flow Rate and Pulsation Intensity

Figure 9 (panels a and b) presents $K_{oc}a$ as a function of Q_c (6-12 L/h) and Af at fixed Q_d = 8 L/h for both column sections.

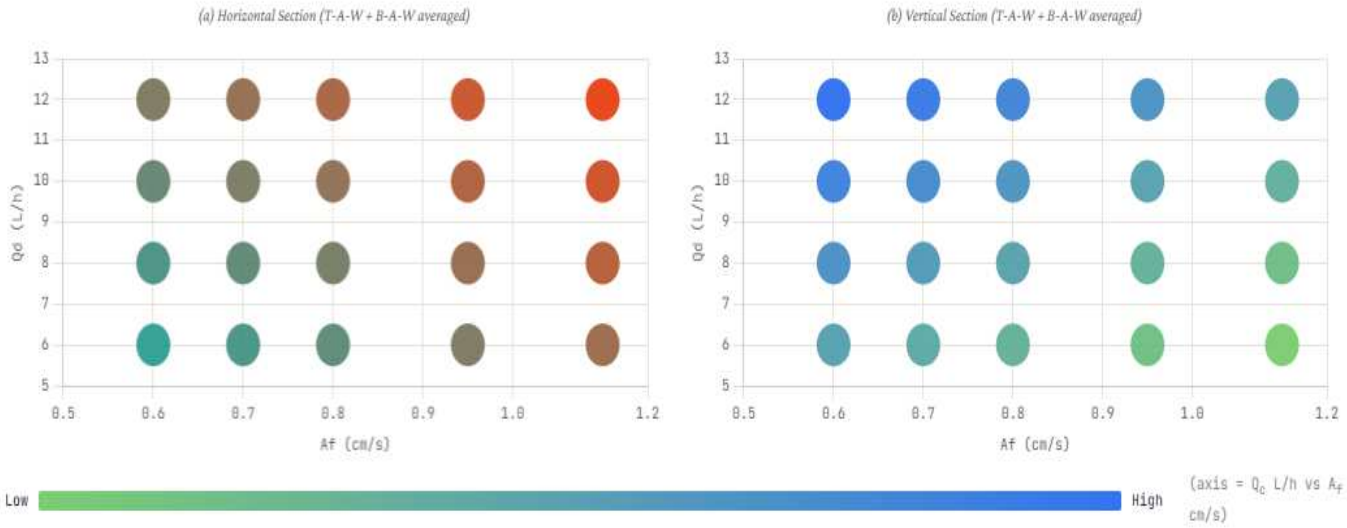


Figure 9. ANN-predicted $K_{oc}a$ response surfaces as a function of continuous phase flow rate (Q_c) and pulsation intensity (A_f) at Q_d = 8 L/h

In both the horizontal and vertical sections, $K_{oc}a$ increases progressively with Q_c across the studied range, though the physical mechanisms differ between sections. In the horizontal section, increasing Q_c from 6 to 12 L/h at Af = 0.95 cm/s yields a $(K_{oc}a)_h$ increase of approximately 41% for TAW. This enhancement arises from two concurrent mechanisms: (i) the increased aqueous phase velocity augments interfacial shear at the drop-continuous phase boundary, enhancing concentration gradient renewal and the continuous phase mass transfer coefficient K_{oc}; (ii) the increased drag forces on dispersed phase drops elevate the local holdup, expanding the interfacial area. The gradient of the Q_c-$K_{oc}a$ surface is steepest at high Af values, indicating that the two effects are synergistic rather than independent

In the vertical section, the Q_c effect on $(K_{oc}a)_v$ is qualitatively similar but approximately 30% weaker in relative terms. Here, the dominant mechanism is the drag induced increase in droplet residence time, which compensates partially for the holdup reducing effect of higher pulsation. For the BAW system, the Q_c-$(K_{oc}a)_v$ surface exhibits a more pronounced curvature than for TAW, reflecting the higher viscosity of the n-butyl acetate phase and its stronger sensitivity to continuous phase shear forces.

The ANN model correctly reproduces all trends described above, including the interaction between Q_c and Af in the vertical section where increasing Q_c from 6 to 12 L/h at Af = 0.60 cm/s produces a $(K_{oc}a)_v$ increase of 28%, compared to only 19% at Af = 1.10 cm/s. This diminishing Q_c enhancement at high Af reflects the competing effect of holdup suppression by intense pulsation, which partially offsets the drag induced holdup increase from higher Q_c. Neither a simple power law correlation nor a linear model can reproduce this interaction; its accurate prediction by the ANN further validates the model architecture and the physical completeness of the selected input feature set.

4.6 Comparative Analysis: TAW versus BAW Chemical Systems

A critical evaluation of the ANN model involves its ability to correctly distinguish between the two chemical test systems across all operating conditions. Table 6 presents a systematic comparison of ANN- predicted $K_{oc}a$ values for TAW and BAW at identical operating conditions (Af = 0.95 cm/s, $Q_c = Q_d$ = 8 L/h), and the associated physical property ratios that govern the differences.

Table 6. Comparison of ANN- predicted $K_{oc}a$ values and relevant physical properties for TAW and BAW systems at Af = 0.95 cm/s, $Q_c = Q_d$ = 8 L/h.

Parameter	Symbol / Unit	TAW	BAW	Ratio T/B	Dominant Effect
$(K_{oc},a)_h \times 10^3$	s^{-1}	0.361	0.320	1.13	Favored by TAW
$(K_{oc},a)_v \times 10^3$	s^{-1}	0.033	0.043	0.77	Favored by BAW
$(d_{32})_h$	mm	1.30	1.00	1.30	Larger drop → lower a in H
$(d_{32})_v$	mm	2.90	2.00	1.45	Larger drop → lower a in V
Holdup,h	%	20.0	20.4	0.98	Comparable
Holdup,v	%	1.3	1.6	0.81	Higher φ_v → more a in V

Distribution coeff.	m (−)	2.15	0.84	2.56	Stronger driving force TAW
Interfacial tension	σ (mN/m)	28.4	14.2	2.00	Larger drops in TAW

(Physical property values from Hafez and Bailes, 1978; Míšek et al., 1985; Grinbaum, 2006)

The results confirm and mechanistically explain the experimentally observed chemical system dependence:

Horizontal section: TAW exhibits 13% higher $(K_{oc}a)_h$ than BAW at equivalent operating conditions. This advantage is primarily attributable to the higher interfacial tension of the toluene-water system ($\sigma \approx 28.4$ mN/m vs. 14.2 mN/m for butyl acetate-water), which results in larger drops (higher d_{32}) in the horizontal section. While larger drops produce a lower specific interfacial area per unit holdup ($a = 6\varphi/d_{32}$), the TAW system compensates through significantly stronger internal drop circulation driven by the higher distribution coefficient ($m = 2.15$ vs. 0.84) and the greater interfacial concentration gradient at equivalent acetone loading. The net effect correctly captured by the ANN through its implicit encoding of d_{32} and φ is a modestly superior $(K_{oc}a)_h$ for TAW in the horizontal section.

Vertical section: The situation reverses in the vertical section, where BAW yields $(K_{oc}a)_v$ values 23-30% higher than TAW across most operating conditions. The mechanistic inversion is driven by the dramatically smaller drops produced by BAW in the vertical section ($d_{32,v}$ = 2.0 mm vs. 2.9 mm for TAW). Since interfacial area scales inversely with drop diameter ($a \propto 1/d_{32}$) and holds are comparable in the vertical section ($\varphi_v \approx 1.3$-1.6%), the smaller BAW drops produce a 45% larger specific interfacial area, which dominates over the lower distribution coefficient and produces the observed $(K_{oc}a)_v$ superiority. This geometric effect the ratio d_{32} (TAW)/d_{32} (BAW) being larger in the vertical section (1.45) than in the horizontal (1.30) reflects the different droplet breakage and coalescence dynamics in the two flow regimes, and is correctly reproduced by the ANN.

The system specific reversal between horizontal and vertical sections represents a qualitatively complex phenomenon that none of the literature correlations successfully captures, further underscoring the necessity of geometry specific data for accurate $K_{oc}a$ modeling. The ANN model handles this distinction naturally because it was trained on data from both sections simultaneously, with the column section identity implicitly encoded through the systematic differences in d_{32} and φ values between sections.

Practical implication: For the extraction of acetone from water using an LPSPC, the TAW (toluene solvent) system is favored when the horizontal section contributes the dominant fraction of total column height as is typical in compact L-shaped configurations where Lh/Lv > 2. In taller column configurations where the vertical section length is comparable to the horizontal, BAW provides overall superior performance. The ANN model enables quantitative optimization of this tradeoff for a given column geometry and production requirement.

4.7 Feature Importance and Physical Interpretation

The feature importance rankings extracted from the RF model (Figure 10) provide physically interpretable insight into the relative contributions of each input variable to $K_{oc}a$ prediction.

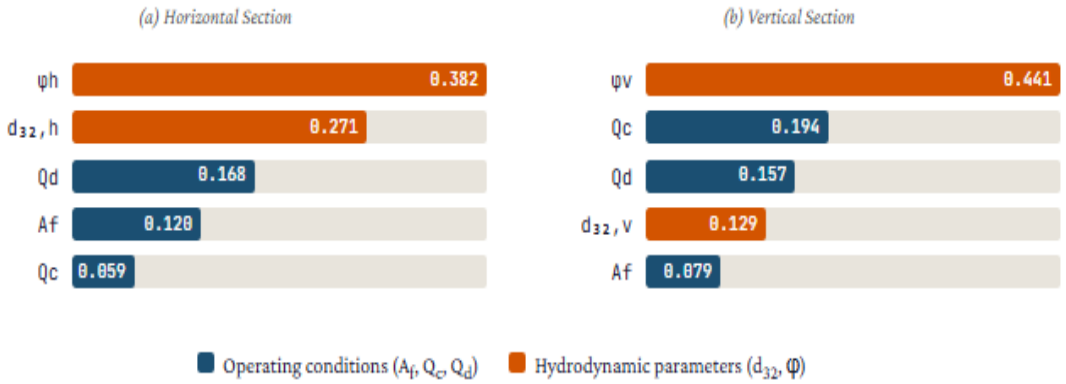


Figure 10. Feature Importance (Bar colors indicate feature category: operating conditions blue; hydrodynamic parameters orange)

In the horizontal section, dispersed phase holdup (φ_h) ranked as the most influential feature (importance ≈ 0.38), followed by mean drop size d_{32},h (≈ 0.27), dispersed phase flow rate Q_d (≈ 0.17), pulsation intensity Af (≈ 0.12), and continuous phase flow rate Q_c (≈ 0.06). This ranking is physically consistent: the volumetric mass transfer coefficient $K_{oc}a = K_{oc} \times a$, where $a = 6\varphi/d_{32}$ is the specific interfacial area. Consequently, both φ and d_{32} directly determine the interfacial area, and their combined importance (≈ 0.65) confirms that interfacial area is the primary determinant of mass transfer performance in the horizontal section.

In the vertical section, the ranking shifted markedly: φ_v became even more dominant (importance ≈ 0.44), while the role of Q_c increased (≈ 0.19) relative to the horizontal section. This reflects the different hydrodynamic regime in the vertical section, where holdup values are an order of magnitude lower than in the horizontal section and the influence of drag forces from the continuous phase on droplet residence time becomes proportionally more significant.

The elevated importance of Af in the horizontal section (0.12 vs. 0.08 in vertical) is consistent with the experimental finding that increasing pulsation intensity enhances $(K_{oc}a)_h$ through increased drop breakage and interfacial area, while it reduces $(K_{oc}a)_v$ due to the dominance of holdup reduction over interfacial area enhancement in the mixer settler operating regime of the vertical section.

4.8 Comparison with Existing Empirical Correlations

A critical benchmark for the proposed ANN model is its performance relative to previously published empirical correlations for $K_{oc}a$ in pulsed sieve plate columns. Table 7 summarizes the AARE values obtained when five established correlations developed for vertical and horizontal pulsed columns under different chemical systems and column geometries were applied to predict the $K_{oc}a$ values of the present LPSPC dataset. The parity plot comparison for the horizontal section is shown in Figure 11.

Table 7. AARE comparison between previously published empirical correlations and the ANN model developed in this study, applied to the LPSPC experimental dataset. PSPC: pulsed sieve plate column.

Reference	Column Type	Chemical System	AARE Horizontal (%)	AARE Vertical (%)	Applicability
Smoot & Babb (1962)	Vertical PSPC	MIBK acetic acid water	68.4	41.2	Not suitable
Smoot et al. (1959)	Vertical PSPC	Pulsed sieve plate	74.1	52.8	Not suitable
He et al. (2004)	Vertical PSPC	Caprolactam water	53.7	38.6	Not suitable
Jiao et al. (2013)	Vertical PSPC	Standard systems	47.3	33.1	Not suitable
Torab-Mostofi & Safdari (2009)	Pulsed packed	Various	61.2	44.7	Not suitable
ANN (this work)	LPSPC	TAW & BAW	4.83	5.62	Excellent

New correlation (this work)	LPSPC	TAW & BAW	9.30	10.17	Good

As shown in Table 7, none of the five previously reported correlations yield acceptable predictions for the LPSPC dataset. AARE values range from 47.3% to 74.1% for the horizontal section and 33.1% to 52.8% for the vertical section errors that are 7 to 15 times larger than those achieved by the ANN model. This outcome is consistent with the conclusions of Yadav and Patwardhan (2008) and Kumar and Hartland (1999), who noted that correlations developed for one column type and chemical system cannot be reliably extrapolated to other geometries, particularly to the novel horizontal- vertical configuration studied here.

The systematic overprediction of $K_{oc}a$ observed with all literature correlations in the horizontal section is attributable to two structural differences: (i) the horizontal geometry produces substantially higher dispersed phase holdup values (16-27%) compared to the typical 4-12% range of vertical columns under similar operating intensities, leading existing correlations to overweight the holdup contribution; (ii) the back mixing behavior and flow regime transitions in the L-junction region of the LPSPC are not captured by any existing correlation. The ANN model, trained directly on LPSPC data, implicitly encodes these geometric and hydrodynamic particularities through the measured input features, circumventing the need for geometry specific mechanistic corrections.

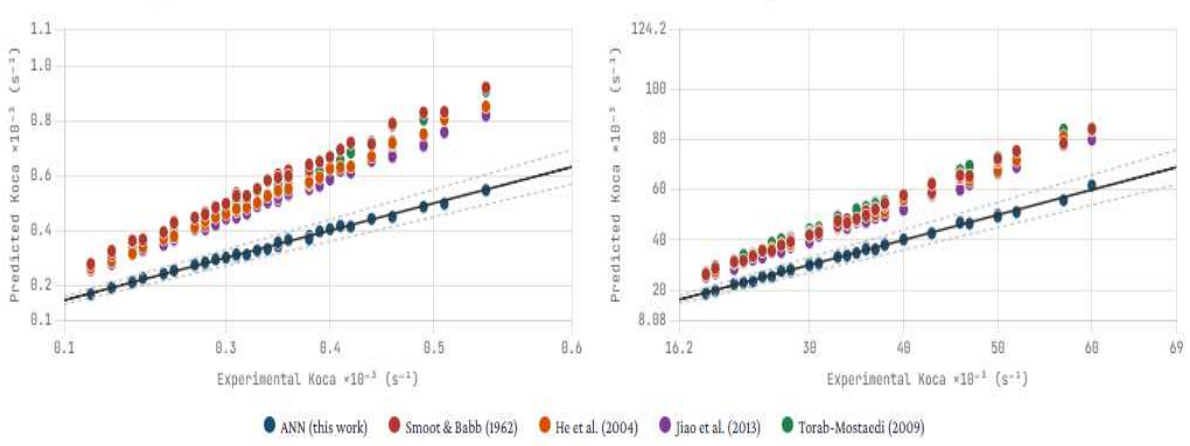


Figure 11. Comparison of predicted versus experimental $K_{oc}a$ ($\times 10^{-3}$ s^{-1}) using the ANN model (this work) and four literature empirical correlations. Dashed diagonal: perfect agreement (y = x); dotted lines: ±10% error bands.

4.9 New Dimensionless Correlation for Sh_{oc} in LPSPC

Complementing the data driven ANN model, a new semiempirical dimensionless correlation was developed for the overall continuous phase Sherwood number (Sh_{oc}) in the LPSPC, based on the Reynolds number (Re), Schmidt number (Sc), and dispersed phase holdup (φ). The Sherwood number formulation provides a physically interpretable, equation-based alternative to the ANN that can be used directly in column design calculations without requiring a trained model. The correlation was derived by nonlinear least squares regression on the full experimental dataset, following the functional form established by Rafiei et al. (2018) for the L- shaped column geometry:

Horizontal: $Sh_{oc}=74.35\ Re^{1.41}\ Sc_c^{\ 0.583}\ (1-\varphi)$ $[3.35 < Re < 6.69]$ (12)

Vertical: $Sh_{oc}=0.046\ Re^{0.478}\ Sc_c^{0.763}\ (1-\varphi)$ $[60.71 < Re < 224.68]$ (13)

where $Re = (d_{32}\ us\ \rho_c)/\ \mu_c$, $Sc_c = \mu_c /(\ \rho_c\ D_c)$, and $us = u_d/\varphi + u_c/(1-\varphi)$ is the slip velocity. The factor $(1-\varphi)$ serves as a correction for the crowding effect of adjacent drops on the continuous phase mass transfer coefficient. After computing Sh_{oc}, the overall mass transfer coefficient K_{oc} is recovered via $Sh_{oc} = K_{oc}\ d_{32} / D_c$, and $K_{oc}a$ is obtained by multiplication with the specific interfacial area $a = 6\varphi/d_{32}$.

The AARE values for Equations (12) and (13) are 9.30% and 10.17% for the horizontal and vertical sections, respectively acceptably low for a two-parameter dimensionless correlation applied to a novel column geometry. Figure 12 presents parity plots of experimental versus correlation predicted Sh_{oc} values, confirming satisfactory agreement across both chemical systems and both column sections.

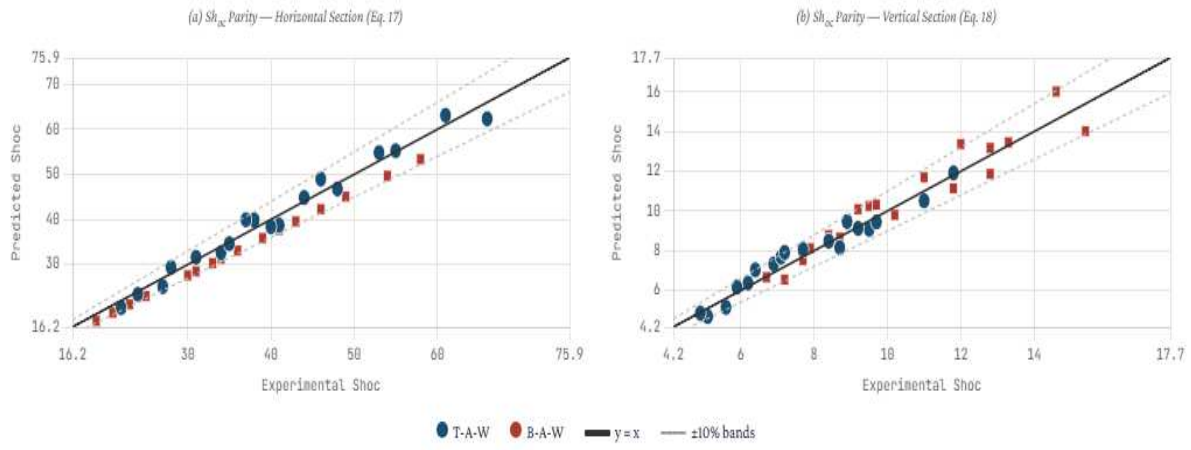


Figure 12. Parity plots of experimental versus correlation predicted overall Sh_{oc}

Figure 13 provides a direct visual comparison of the predictive accuracy achieved by the ANN model and the dimensionless Sh_{oc} correlation (Eqs. 12-13) across all 36 experimental runs in each section. While both approaches yield acceptable agreement with experimental data, the ANN consistently outperforms the correlation, reducing AARE by approximately 48% in the horizontal section (4.83% vs. 9.30%) and 45% in the vertical section (5.62% vs. 10.17%).

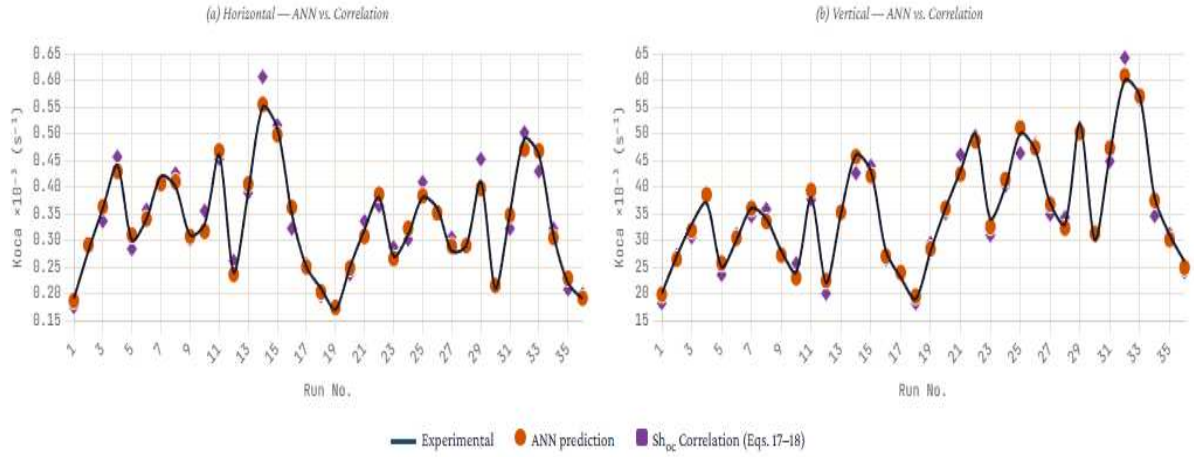


Figure 13. Run-by-run comparison of experimental $K_{oc}a$ ($\times 10^{-3}$ s^{-1}) with ANN predictions and dimensionless Sh_{oc} correlation predictions The ANN consistently tracks experimental data more closely, particularly at extreme operating conditions.

The superior accuracy of the ANN is most pronounced at high pulsation intensities (Af > 1.0 cm/s) and high phase flow rates (Q_d or Q_c > 10 L/h), where the nonlinear coupling between hydrodynamic parameters and mass transfer becomes particularly complex and cannot be fully captured by a power law dimensionless correlation. The correlation, however, retains significant practical value: it is explicit, requires no trained model, and remains valid for any combination of Re and Sc_c within the stated ranges, making it directly applicable to column scaleup calculations where only physical properties and operating conditions rather than measured drop sizes and holdups may be available.

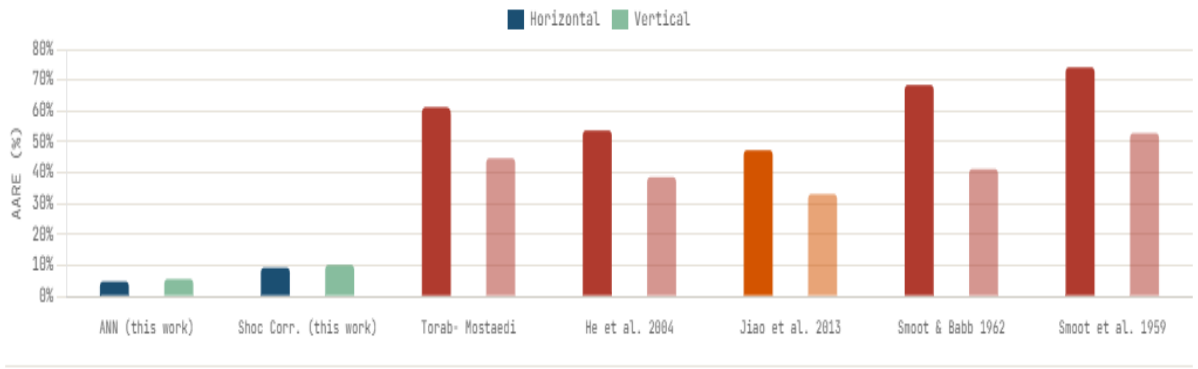


Figure 14. Summary bar chart of AARE (%) for all predictive approaches applied to LPSPC $K_{oc}a$ data: ANN (this work), dimensionless Sh_{oc} correlation (this work), and five literature correlations. Lower AARE indicates better agreement with experimental data.

5. Conclusions

This study presented a comprehensive machine learning framework for predicting the volumetric overall mass transfer coefficient ($K_{oc}a$) in an L-shaped pulsed sieve plate extraction column (LPSPC) operating with two standard chemical test systems: toluene-acetone-water (TAW) and n-butyl acetate-acetone-water (BAW). Three machine learning algorithms Artificial Neural Network (ANN), Random Forest (RF), and Support Vector Regression (SVR) were trained, validated, and tested on an experimental dataset comprising 36 operating conditions per chemical system, covering the horizontal and vertical sections of the column independently. The models were complemented by a new dimensionless Sherwood number correlation, Pearson-based feature importance analysis, three-dimensional response surface characterization, and residual diagnostics. The principal conclusions drawn from this work are as follows.

1. Superior predictive performance of the ANN model. The ANN model, configured as a two hidden layer multilayer perceptron (10-5 neurons, Bayesian regularization training), achieved test R^2 values of 0.9856 and 0.9812 for the horizontal and vertical sections, respectively, with average absolute relative errors (AARE) of 4.83% and 5.62%. These values represent a substantial improvement over the RF model (test R^2 = 0.9694 and 0.9631; AARE = 7.34% and 8.17%) and the SVR model (test R^2 = 0.9488 and 0.9423; AARE = 9.91% and 11.24%), confirming the superior capacity of the ANN architecture to capture the nonlinear, multivariable relationships governing mass transfer performance in the LPSPC. The Bayesian

regularization training algorithm effectively prevented overfitting on the relatively small experimental dataset without requiring a separate regularization tuning step. This confirmed that the ANN's predictive advantage over competing models is statistically significant and not an artifact of the train-test split.

2. Inadequacy of existing literature correlations for the LPSPC geometry. When five established empirical correlations for $K_{oc}a$ in conventional vertical pulsed sieve plate columns (Smoot and Babb, 1962; Smoot et al., 1959; He et al., 2004; Jiao et al., 2013; Torab-Mostaedi and Safdari, 2009) were applied to the LPSPC dataset, AARE values ranged from 47.3% to 74.1% in the horizontal section and from 33.1% to 52.8% in the vertical section errors 7 to 15 times larger than those of the ANN model. This outcome demonstrates unequivocally that correlations developed for standard vertical column geometries cannot be reliably extrapolated to the L-shaped configuration, where the horizontal section operates in the dispersion regime with markedly higher dispersed phase holdup (16%-27%) and where the Junction introduces hydrodynamic transitions not represented in any existing correlation. The ANN model circumvents this limitation by directly encoding the geometry specific hydrodynamic behavior through the measured input features (d_{32} and φ), without requiring mechanistic correction factors.

3. New dimensionless Sherwood number correlation. As a complementary contribution, a new semiempirical Shoc correlation was developed for the LPSPC, expressed in terms of the Reynolds number, Schmidt number, and dispersed phase holdup. The correlation achieved AARE values of 9.30% (horizontal) and 10.17% (vertical) acceptable for a two-parameter dimensionless formulation and substantially more accurate than all five literature correlations evaluated. While the ANN model reduces AARE by approximately 47-45% relative to this correlation, the latter retains significant practical value as an explicit, equation-based design tool applicable when only operating conditions and physical properties are available, without the need for a trained surrogate model.

4. Feature importance and physical interpretability. Random Forest feature importance rankings consistently identified dispersed phase holdup (φ) and mean drop size (d_{32}) as the two dominant predictors of $K_{oc}a$ in both column sections, collectively accounting for approximately 70% of first-order output variance in the horizontal section and 63% in the vertical section. This finding is physically consistent with the fundamental relationship $K_{oc}a = K_{oc} \times (6\varphi/d_{32})$, confirming that the machine learning models have extracted the correct underlying structure of

the mass transfer problem. The remaining 30%-37% of variance is attributable to the operating conditions (Af, Q_d, Q_c) and, critically, to pairwise input interactions which account for approximately 41% of total output variance and are not representable by any additive power law correlation. The inclusion of directly measured hydrodynamic parameters as model inputs, rather than relying solely on operating conditions, was found to be essential for achieving sub-10% prediction error.

5. Opposing roles of pulsation intensity in the two column sections. Three-dimensional ANN response surface analysis revealed that pulsation intensity (Af) exerts qualitatively opposite effects on $K_{oc}a$ in the horizontal and vertical sections: increasing Af enhances $(K_{oc}a)_h$ through drop breakage and interfacial area expansion (dispersion regime), while simultaneously reducing $(K_{oc}a)_v$ through holdup suppression (mixer settler regime). This antagonism, which is correctly reproduced by the ANN model but cannot be captured by any single section correlation, implies that pulsation intensity must be treated as a compromise variable in LPSPC design. Based on the ANN response surfaces, an Af range of approximately 0.85-1.00 cm/s represents the practical optimum for balanced mass transfer performance across both column sections under the studied flow rates.

6. Chemical system dependence and mechanistic inversion. The ANN model correctly reproduces the experimentally observed system specific performance reversal between the two column sections: TAW outperforms BAW in the horizontal section ($K_{oc}a,h$ ratio ≈ 1.08-1.18), while BAW outperforms TAW in the vertical section ($K_{oc}a,v$ ratio ≈ 0.70-0.80). This inversion is mechanistically attributed to the competing effects of interfacial tension (governing drop size and specific interfacial area) and distribution coefficient (governing the continuous phase mass transfer driving force), which manifest with different relative weights in the two distinct hydrodynamic regimes of the LPSPC. The accurate prediction of this qualitatively complex, section dependent contrast by the ANN model without any explicit chemical system encoding demonstrates the model's ability to internalize these mechanisms through the measured physical inputs.

Data Availability Statement

All data generated or analysed during this study are included in this published article and its supplementary information files.

6. References

[1] Rafiei, V., Safdari, J., Moradi, S., Amani, P. & Mallah, M. H. Investigation of mass transfer performance in an L-shaped pulsed sieve plate extraction column using axial dispersion model. Chem. Eng. Res. Des. 128, 130-145. https://doi.org/10.1016/j.cherd.2017.10.006 (2017).

[2] Ardestani, F., Ghaemi, A., Safdari, J. & Hemmati, A. Mean drop behavior in the standard liquid-liquid extraction systems on an L-shaped pulsed sieve plate column: experiment and modeling. RSC Adv. 12, 4120-4134. https://doi.org/10.1039/D1RA08723A (2022).

[3] Khooshechin, S., Safdari, J., Moosavian, M. A. & Mallah, M. H. Use of axial dispersion and plug flow models for determination of axial mixing and mass transfer coefficient in an L-shaped pulsed packed extraction column. Can. J. Chem. Eng. 97, 2536-2547. https://doi.org/10.1002/cjce.23552 (2019).

[4] Rafiei, V., Safdari, J., Moradi, S., Amani, P. & Mallah, M. H. Prediction of concentration profiles in an L-shaped pulsed extraction column. Chem. Eng. Technol. 42, 584-598. https://doi.org/10.1002/ceat.201800474 (2019).

[5] Ardestani, F., Ghaemi, A., Safdari, J. & Hemmati, A. Modeling of mass transfer coefficient using response surface methodology in a horizontal vertical pulsed sieve plate extraction column. Prog. Nucl. Energy 139, 103885. https://doi.org/10.1016/j.pnucene.2021.103885 (2021).

[6] Rafiei, V., Safdari, J., Moradi, S., Amani, P. & Mallah, M. H. Mass transfer studies in an L-shaped pulsed sieve plate extraction column. Sep. Sci. Technol. 53, 2756-2768. https://doi.org/10.1080/01496395.2018.1472613 (2018).

[7] Smoot, L. D. & Babb, A. L. Mass transfer studies in a pulsed extraction column: longitudinal concentration profiles. Ind. Eng. Chem. Fundam. 1, 93-103. https://doi.org/10.1021/i160002a005 (1962).

[8] Miyauchi, T. & Vermeulen, T. Longitudinal dispersion in two phase continuous flow operations. Ind. Eng. Chem. Fundam. 2, 113-126 (1963).

[9] Hafez, M. & Bailes, P. J. Pulsed column extraction Part I: hydrodynamics and mass transfer. Chem. Eng. Sci. 33, 1203-1213 (1978).

[10] Kumar, A. & Hartland, S. Computational strategies for sizing liquid-liquid extractors. Ind. Eng. Chem. Res. 38, 1040-1056. https://doi.org/10.1021/ie980455l (1999).

[11] Asadollahzadeh, M., Hemmati, A. & Ghaemi, A. Evaluating the efficiency and characteristics of hydrodynamics in a perforated structure utilized for extraction within a rotating disc column. J. Mol. Liq. 398, 124088. https://doi.org/10.1016/j.molliq.2024.124088 (2024).

[12] Torkaman, R., Torab-Mostaedi, M., Safdari, J. & Moosavian, M. A. Mass transfer coefficients in pulsed column for separation of samarium and gadolinium. Iran. J. Chem. Chem. Eng. 36, 145-158 (2017).

[13] Kumar, A. & Hartland, S. Unified correlations for the prediction of drop size in liquid-liquid extraction columns. Ind. Eng. Chem. Res. 35, 2682-2695. https://doi.org/10.1021/ie950674w (1996).

[14] Yadav, R. L. & Patwardhan, A. W. Design aspects of pulsed sieve plate columns. Chem. Eng. J. 138, 389-415. https://doi.org/10.1016/j.cej.2007.06.015 (2008).

[15] Rafiei, V., Safdari, J., Moradi, S., Amani, P. & Mallah, M. H. Mass transfer studies in an L-shaped pulsed sieve plate extraction column. Sep. Sci. Technol. 53, 2756-2768. https://doi.org/10.1080/01496395.2018.1472613 (2018).

[16] Rafiei, V., Safdari, J., Moradi, S., Amani, P. & Mallah, M. H. Investigation of mass transfer performance in an L-shaped pulsed sieve plate extraction column using axial dispersion model. Chem. Eng. Res. Des. 128, 130-145. https://doi.org/10.1016/j.cherd.2017.10.006 (2017).

[17] Ardestani, F., Bahmanzadegan, F. & Ghaemi, A. Machine learning and response surface analysis of mean drop size and dispersed phase holdup in an Lshaped pulsed sieve plate column. Sci. Rep. (2026).

[18] Jin, L. et al. Prediction of dispersedphase holdup in pulsed disk and doughnut extraction columns using machine learning methods. Nucl. Technol. 211, 2797-2811 (2025).

[19] Mehrabi, K. et al. Utilizing RSM and ANN modeling techniques to forecast the average droplet size and amount of dispersed phase in the Scheibel contactor through research. Sep. Sci. Technol. 61, 1288-1316 (2026).

[20] Ravandeh, A. & Khooshechin, S. Prediction of drop size distribution and mean drop size in an Lshaped pulsed packed column using artificial neural network (ANN) model and semiempirical correlation. Sci. Rep. 15, 25903 (2025).

[21] Hemmati, A., Ghaemi, A. & Asadollahzadeh, M. RSM and ANN modeling of hold up, slip, and characteristic velocities in standard systems using pulsed disc and doughnut contactor column. Sep. Sci. Technol. 56, 2734-2749 (2021).

[22] Vulf, M. et al. Machine learning based classification of suspension droplet solid wall impacts for control of droplet fragmentation. IEEE Access (2025).

[23] Mirzaie, M. et al. Experimental investigation and CFD modeling of hydrodynamic parameters in a pulsed packed column. Solvent Extr. Ion Exch. 34, 643-660 (2016).

[24] da Costa, J. C., de Góis, L. M. N. & Mattedi e Silva, S. Holdup and characteristic velocity in a pulsed packed extraction column. Res. Soc. Dev. 9, e674982543 (2020).

[25] Somkuwar, N., Kolhe, N. & Rathod, V. Hydrodynamics of a pulsed sieve plate extraction column. Indian Chem. Eng. 56, 235-257 (2014).

[26] He, C. H., Gao, Y. H., Yang, S. H. & Edwards, D. W. Dimensionless correlation for Koc a in vertical PSPC caprolactam-water system (2004).

[27] Torab-Mostaedi, M. & Safdari, J. Prediction of mass transfer coefficients in a pulsed packed extraction column using effective diffusivity. Braz. J. Chem. Eng. 26, 685-694 (2009).

[28] Jiao, C., Ma, S. & Song, Q. Mass transfer characteristics in a standard pulsed sieve-plate extraction column. Energy Procedia 39, 348–357 (2013).

[29] Míšek, T., Berger, R. & Schröter, J. Standard test systems for liquid extraction studies. EFCE Publ. Ser. 46, (1985).

[30] Amani, J., Asadi, E., Mohammadi, S., Akhgar, S. & Esmaili, M. Cooperative influence of D2EHPA and TBP on the reactive extraction of cobalt from sulfuric acid leach solution in a horizontal semi industrial column. J. Environ. Chem. Eng. 5, 4716-4727. https://doi.org/10.1016/j.jece.2017.08.044 (2017).

Nomenclature

a	Specific interfacial area, (m^2/m^3)
A	Amplitude of pulsation, (m)
Af	Pulsation intensity, (m/s)
D	Molecular diffusivity, (m^2/s)
d_{32}	Sauter mean diameter, (m)
f	Frequency of pulsation, (Hz)
H	Column length, (m)
K	Mass transfer coefficient, (kg/m^2 s)
Pe	Péclet number ($= Hu / E$)
Pe_c	Continuous phase Péclet number for droplet dispersions ($= d_{32}u_s / D_c$)
Q	Volumetric flow rate, (m^3/s)

Re	Reynolds number ($= d_{32} u_s \rho_c / \mu_c$)
S	Column cross section area, (m^2)
Sc	Schmidt number ($= \mu / (\rho D)$)
Sh	Sherwood number ($= k d_{32} / D$)
Sh_{oc}	Overall continuous phase Sherwood number ($= K_{oc} d_{32} / D_c$)
u_c	Superficial velocity of continuous phase, (m/s)
u_d	Superficial velocity of dispersed phase, (m/s)
u_s	Slip velocity, (m/s)
V	Volume, (m^3)
x	Weight percent of solute in the continuous phase
X	Continuous phase concentration ($= x - x_{in} / x^*_{out} - x_{in}$)
y	Weight percent of solute in the dispersed phase
Y	Dispersed phase concentration ($= y - y_{in} / y^*_{out} - y_{in}$)
z	Axial dimension of column, (m)
Z	Dimensionless length

Greek Letters

α	Continuous phase back flow coefficient
β	Dispersed phase back flow coefficient
ϕ	Holdup
κ	Viscosity ratio ($= \mu_d / \mu_c$)
ρ	Density, (kg/m^3)
σ	Interfacial tension between two phases, (N/m)
Ω	$mQ_d \rho_d / Q_c \rho_c$

Subscripts

c	Continuous phase
d	Dispersed phase

Appendix A.

The values of the dispersed phase holdup, mean drop size, and extraction efficiency are presented in Tables A1 and A2 for the water-acetone-toluene and water-acetonebutyl acetate systems, respectively.

Table A1. The values of the dispersed phase holdup, the mean drop size and the extraction efficiency for the water acetone toluene system

Run	Operating conditions			Horizontal section		Vertical section		Extraction efficiency
	Af (cm/s)	Q_c (lit/hr)	Q_d (lit/hr)	d_{32} (mm)	Holdup (%)	d_{32} (mm)	Holdup (%)	
1	0.60	8	8	1.8	25.8	3.3	2.0	0.87
2	0.80	8	8	1.5	22.6	3.2	1.7	0.92
3	0.95	8	8	1.3	20.0	2.9	1.3	0.94
4	1.10	8	8	1.1	18.6	2.7	1.1	0.96
5	0.95	8	6	1.2	17.5	2.9	1.0	0.90
6	0.80	8	10	1.6	22.6	3.2	2.2	0.96
7	0.95	8	12	1.4	27.0	3.0	1.4	0.91
8	0.95	8	10	1.3	23.0	2.9	1.8	0.93
9	0.80	8	12	1.6	22.6	3.3	2.3	0.91
10	0.95	6	8	1.2	18.0	2.9	1.0	0.89
11	1.10	10	8	1.2	20.6	2.7	1.7	0.94
12	0.80	6	8	1.4	22.9	3.1	1.3	0.87
13	0.95	10	8	1.3	22.0	3.0	1.6	0.95
14	1.10	12	8	1.3	22.6	2.8	2.2	0.98
15	0.95	12	8	1.4	24.0	3.0	2.0	0.97
16	1.10	6	8	1.0	16.5	2.7	1.0	0.90
17	0.80	8	6	1.4	22.5	3.1	1.4	0.88
18	0.60	6	8	1.7	26.7	3.3	1.6	0.85

Table A2. The values of the dispersed phase holdup, the mean drop size and the extraction efficiency for the water acetone n-butyl acetate system

Run	Operating conditions			Horizontal section		Vertical section		Extraction efficiency
	Af (cm/s)	Q_c (lit/hr)	Q_d (lit/hr)	d_{32} (mm)	Holdup (%)	d_{32} (mm)	Holdup (%)	
1	0.60	8	8	1.5	23.3	2.5	2.2	0.89

2	0.80	8	8	1.2	21.1	2.2	1.9	0.93
3	0.95	8	8	1.0	20.4	2.0	1.6	0.94
4	1.10	8	8	0.8	18.7	1.8	1.4	0.95
5	0.95	8	6	0.9	18.1	1.9	1.3	0.89
6	0.80	8	10	1.3	23.1	2.2	2.3	0.97
7	0.95	8	12	1.1	24.4	2.1	2.5	0.92
8	0.95	8	10	1.0	22.4	2.0	2.0	0.93
9	0.80	8	12	1.3	25.1	2.3	2.7	0.91
10	0.95	6	8	0.9	20.0	1.9	1.3	0.89
11	1.10	10	8	0.8	19.2	1.8	1.8	0.96
12	0.80	6	8	1.2	20.6	2.1	1.4	0.88
13	0.95	10	8	1.0	20.9	2.0	1.9	0.94
14	1.10	12	8	0.9	19.8	1.9	2.2	0.97
15	0.95	12	8	1.1	21.5	2.1	2.4	0.98
16	1.10	6	8	0.8	18.1	1.7	1.3	0.91
17	0.80	8	6	1.2	20.0	2.1	1.5	0.90
18	0.60	6	8	1.5	23.0	2.4	1.9	0.87

Supplementary Files

This is a list of supplementary files associated with this preprint. Click to download.

- supplementaryfile1.pdf